



# Detecting urban changes using phase correlation and $l_1$ -based sparse model for early disaster response: A case study of the 2018 Sulawesi Indonesia earthquake-tsunami

Luis Moya<sup>a,b,\*</sup>, Abdul Muhari<sup>c</sup>, Bruno Adriano<sup>d</sup>, Shunichi Koshimura<sup>a</sup>, Erick Mas<sup>a</sup>, Luis R. Marval-Perez<sup>e</sup>, Naoto Yokoya<sup>d</sup>

<sup>a</sup> International Research Institute of Disaster Science, Tohoku University, Aoba 468-1-E301, Aramaki, Aoba-ku, Sendai 980-8572, Japan

<sup>b</sup> Japan-Peru Center for Earthquake Engineering Research and Disaster Mitigation, National University of Engineering, Tupac Amaru Avenue 1150, Lima 25, Peru

<sup>c</sup> National Disaster Management Authority of Indonesia, Jakarta, Indonesia

<sup>d</sup> Geoinformatics Unit, RIKEN Center for Advance Intelligence Project, Tokyo 103-0027, Japan

<sup>e</sup> Graduate School of Information Science, Tohoku University, 6-6-05 Aramaki Aza Aoba, Aoba-ku, Sendai 980-8579, Japan

## ARTICLE INFO

Edited by Jing M. Chen

### Keywords:

Building damage

Phase correlation

Sparse logistic regression

The 2018 Sulawesi Indonesia earthquake-tsunami

## ABSTRACT

Change detection between images is a procedure used in many applications of remote sensing data. Among these applications, the identification of damaged infrastructures in urban areas due to a large-scale disaster is a task that is crucial for distributing relief, quantifying losses, and rescue purposes. A crucial consideration for change detection is that the images must be co-registered precisely to avoid errors resulting from misalignments. An essential consideration is that some large-magnitude earthquakes produce very complex distortions of the ground surface; therefore, a pair of images recorded before and after a particular earthquake cannot be co-registered accurately. In this study, we intend to identify changes between images that are not co-registered. The proposed procedure is based on the use of phase correlation, which shows different patterns in changed and non-changed areas. A careful study of the properties of phase correlation suggests that it is robust against misalignments between images. However, previous studies showed that, in areas with no-changes, the signal power in the phase correlation is not concentrated in a single component, but rather in several components. Thus, we study the performance of the  $l_1$ -regularized logistic regression classifier to identify the relevant components of phase correlation and learn to detect non-changed and changes areas. An empirical evaluation consisting of identifying the changes between pre-event and post-event images corresponding to the 2018 Sulawesi Indonesia earthquake-tsunami was performed for this purpose. Pairs of visible and near-infrared (VNIR) spectral bands of medium-resolution were used to compute the phase correlation to set feature space. The phase correlation-based feature space consisted of 484 features. We evaluate the proposed procedure using a damage inventory performed from visual inspection of optical images of 0.5-m resolution. A third-party provided the referred inventory. Because of the limitation of medium-resolution imagery, the different damage levels in the damage inventory were merged into a binary class: “changed” and “non-changed”. The results demonstrate that the proposed procedure efficiently reproduced  $85 \pm 6\%$  of the damage inventory. Furthermore, our results identified tsunami-affected areas that were not previously identified by visual inspection.

## 1. Introduction

Estimating the damage to the built environment after a large-scale disaster using remote sensing data has become an important task (Matsuoka and Yamazaki, 2004; Yamazaki and Matsuoka, 2007; Matsuoka and Nojima, 2010; Ghosh et al., 2011; Liu et al., 2013; Gokon et al., 2016; Miura et al., 2016; Liu and Yamazaki, 2017; Karimzadeh

and Mastuoka, 2017; Moya et al., 2018a, 2018b, 2018c; Bai et al., 2018; Moya et al., 2019a, 2019b). The most common approach, termed *change detection*, is employed to identify changes between a pair of images recorded before (pre-event) and after (post-event) an arbitrary disaster. A proper comparison between these two images requires their georeference to have high precision. In order to reduce the effects of distortions and offsets between images, a preliminary process called

\* Corresponding author at: International Research Institute of Disaster Science, Tohoku University, Japan.

E-mail address: [lmoyah@irides.tohoku.ac.jp](mailto:lmoyah@irides.tohoku.ac.jp) (L. Moya).

<https://doi.org/10.1016/j.rse.2020.111743>

Received 18 July 2019; Received in revised form 24 February 2020; Accepted 27 February 2020

Available online 12 March 2020

0034-4257/ © 2020 The Author(s). Published by Elsevier Inc. This is an open access article under the CC BY license (<http://creativecommons.org/licenses/by/4.0/>).

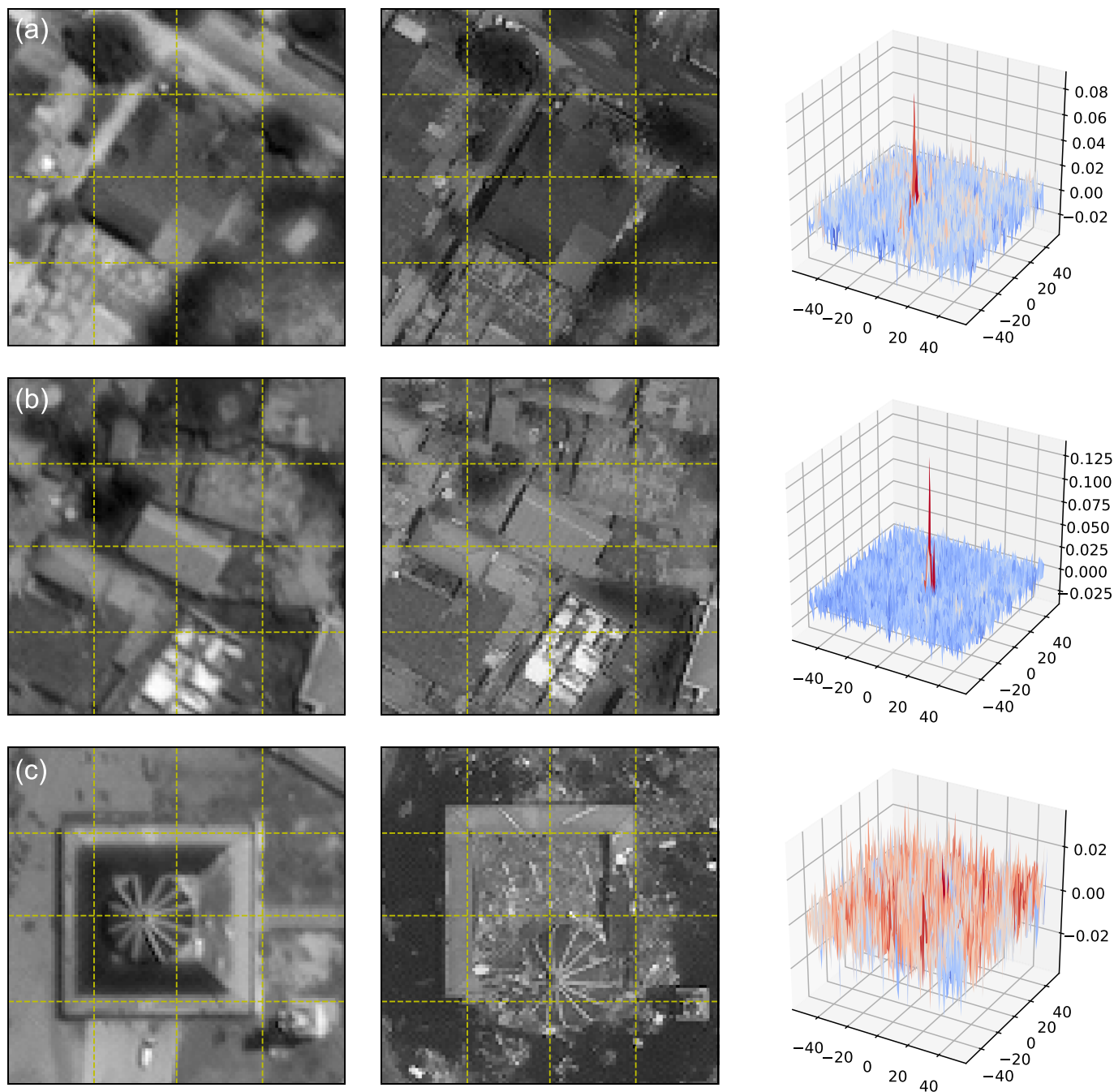


**Fig. 1.** Illustrations of the PCs computed on urban areas. (left) Red-band pre-event optical image recorded on July 4, 2018. (middle) Red-band post-event optical image recorded on October 2, 2018. (right) Computed PC. Grid lines were included to emphasize the offset between both images. The images were downloaded from the DigitalGlobe Open Data Program. Notice the presence of a peak on the PCs computed on non-damaged urban areas (a–b) and the absence of a peak from the PC computed on a damaged urban area (c).

image registration must be applied. Generally, image registration refers to the process of aligning different images of the same scene acquired at different times, at different viewing angles, and/or with different sensors. Initially, image registration required expert intervention to select ground control points (GCPs) manually, a task that can be laborious, time-consuming, and sometimes challenging in low-resolution optical/microwave imagery. Fortunately, to date, various automatic image registration procedures have been proposed (Cole-Rhodes et al., 2003; Wong and Clausi, 2007; Kern and Pattichis, 2007; Goncalves et al., 2011; Xu et al., 2016; Feng et al., 2019). However, the selection of GCPs is still a critical issue in automatic procedures. The number of GCPs is a trade-off problem. A low number of GCPs results in poor registration;

on the other hand, an excessive number of GCPs requires a high computational cost. In general, standard image registration utilizes the offsets measured at GCPs to re-sample one image to align it with the other. Similarity and polynomial warping are standard re-sampling techniques (Canty, 2014). Similarity warping assumes a uniform offset, rotation, and scaling, while polynomial warping performs a polynomial mapping, which produces smooth re-sampling between GCPs. However, complex local distortions cannot be registered.

Recently, image registration techniques have been used to quantify real deformation. Correlation, an essential procedure behind the image registration process, has been recently applied to quantify 2D ground deformation (Rosu et al., 2015). Fang et al. (2016) used phase

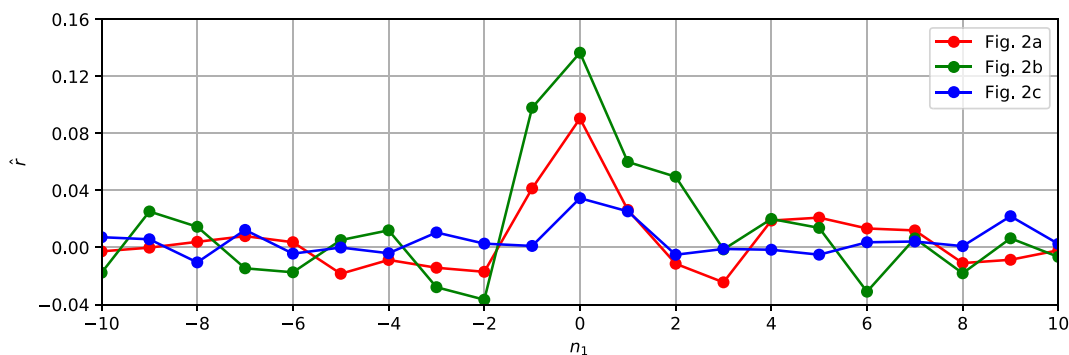


Fig. 2. Cross section of a PC.



Fig. 3. Portion of the urban area of Palu city, Indonesia, captured by DigitalGlobe's sensor on July 4, 2018 (left), and October 2, 2018 (right), that is, before and after the earthquake, respectively. The orange dashed line in the right figure denotes the location of the fault line. The numbers and arrows in yellow denote the magnitude (in meters) and the orientation of the horizontal offset component, respectively. The location of the area is shown in Fig. 5c. (For interpretation of the references to color in this figure legend, the reader is referred to the web version of this article.)

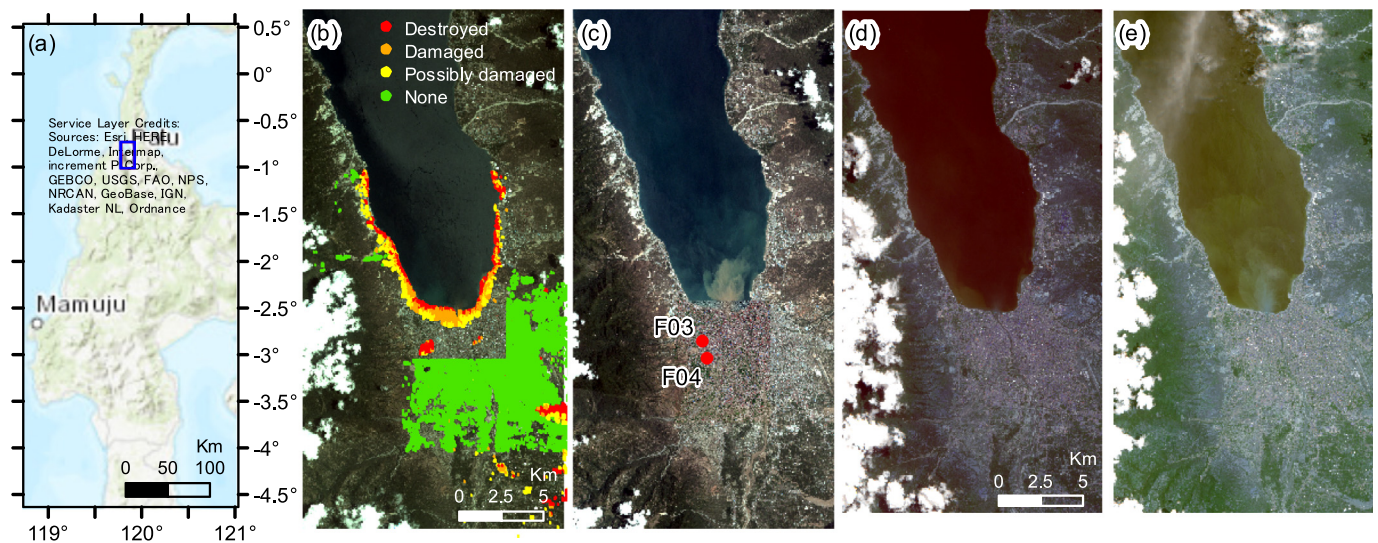


Fig. 4. Illustration of the surface rupture caused by the 2018 Sulawesi Indonesia earthquake in an agricultural field. Left: Illustration of the discontinuity in the linear arrangements of crops due to the fault rupture. Right: Measurement of the deformation across the fault line. Photos provided by Koshimura et al. (2019). The locations of the photos are shown in Fig. 5c.

Table 1

Specifications of the satellite images used in this study.

Satellite constellation	Acquisition date	Spectral bands	Relative Orbit number	Covered area (km <sup>2</sup> )	Resolution (m)
Planet	28/09/2018	VNIR	–	2955	3
Planet	01/10/2018	VNIR	–	1735	3
Sentinel-2	18/08/2018	VNIR	103	10,000	10
Sentinel-2	02/10/2018	VNIR	103	10,000	10



**Fig. 5.** Study area and satellite imagery. (a) Location of the study area, drawn as a blue rectangle, on the western part of Sulawesi, Indonesia. (b) Optical image acquired by Planet on September 28, 2018. The colored marks denote the damage states of buildings provided by Copernicus. (c) Optical image acquired by Planet on October 1, 2018. The red dots labeled F03 and F04 denote the locations of Figs. 3 and 4, respectively. (d) and (e) Optical images acquired by Sentinel-1 on August 18, 2018, and October 2, 2018, respectively. (For interpretation of the references to color in this figure legend, the reader is referred to the web version of this article.)

correlation in synthetic aperture radar (SAR) intensity images to estimate glacier surface motion. Three-dimensional coseismic displacements were computed from Lidar data in Moya et al. (2017). In Stumpf et al. (2017), multiple-pairwise image correlation was employed to detect and monitor slow-moving landslides. Bao et al. (2019) used normalized cross-correlation to compute the slip distribution of the 2018 Mw 7.5 earthquake that struck Palu, Indonesia, and its results were used as evidence of an earthquake source consisting of an early and persistent supershear rupture mechanism. A specific issue arises when collapsed buildings in areas that suffer permanent ground deformation must be identified; a situation associated with large-magnitude earthquakes. The 2011 moment magnitude (Mw) 9 Tohoku-Oki earthquake-tsunami (Ozawa et al., 2011; Liu et al., 2013), the 2016 Mw 7 Kumamoto earthquake (Moya et al., 2017, 2018c), and the 2018 Mw 7.5 Sulawesi Indonesia earthquake-tsunami (Bao et al., 2019) are examples of such scenarios. Mathematical models of the ground deformation caused by an earthquake are based on the combination of two terms: the near-field and far-field terms (Shearer, 2009; Udías et al., 2014). Both terms depend on the distance,  $R$ , to the earthquake source. The far-field term is inversely proportional to  $R$ , whereas the near-field term is, depending on the model, inversely proportional to a power of  $R$ . This means that the near-field term is dominant in areas close to the source, and thus, image registration based on a constant shift or linear transformation might not be sufficient. The most critical issue is, however, when the area of interest contains the fault line associated with the earthquake. A fault line is a planar fracture or discontinuity between rock bodies. When the rupture mechanism is strike-slip motion, prominent offsets are produced with opposite directions on each side of the fault. Such sudden discontinuities cannot be corrected in areas between GCPs because the standard image methods assume smooth transitions.

The features commonly used to detect changes produced by large-scale disasters are computed under the assumption that the images are correctly co-registered. In this manuscript, we propound the search for suitable features for damage detection that might be invariant to offsets and/or distortions. In this way, the image registration processing may be eliminated from the damage mapping processing chain. Intuitively, the most promising candidates are the parameters hidden in the techniques employed for image registration. Image registration is intimately related to change detection. Damage detection looks for changes, whereas image registration looks for similarities. Therefore, in this

study, we evaluate the potential of phase correlation (PC), which is based on the Fourier shift theorem, to identify damage in urban areas. The PC is the inverse discrete Fourier transform of a normalized cross power spectrum computed from a pair of images. A comprehensive review of applications of Fourier-based image correlation on image registration is provided in Tong et al. (2019). If the two images are similar, then the PC will exhibit a prominent peak, whose location indicates the offset of one image with respect to the other. However, here, we are concerned with the existence of such a peak rather than its location. It is assumed, given that the temporal baseline between images is short enough, that urban areas without heavy damage will exhibit a distinctive peak in their PC; otherwise, there will be no peak. As noted elsewhere (Takita et al., 2013; Foroosh et al., 2002), the peak shape, i.e., the peak height and its surrounded values, provides a better-detailed description of the degree of similarity between images rather than only the peak height. Therefore, we use a sparse statistical model, more specifically,  $\ell_1$ -regularized logistic regression, to find the number of components of PC that play an important role in the identification of changes. It is worth noting, the use of PC in remote sensing-based change detection for disaster response is almost negligible. Adriano et al. (2015) used PC to identify damage from microwave imagery. However, their study was limited to the use of the maximum value of the PC. Thus, an innovative aspect of our study is the analysis of the complete signal of the PC through sparse modeling, and the results suggest that not only the maximum value of the PC-array contains valuable information to identify damage from remote sensing data.

The remainder of this paper is organized as follows. The next chapter introduces the phase correlation (PC) technique to some extent, emphasizing its effect on a discrete domain and its application to collapsed and non-collapsed buildings. Chapter 3 provides a glimpse of the  $\ell_1$ -regularized logistic regression classifier. In chapter 4, the performance of the proposed method is evaluated on the identification of changes between pairs of images corresponding to the 2018 Mw 7.5 Sulawesi earthquake-tsunami. Finally, our conclusions are drawn in Chapter 5.

## 2. The phase correlation (PC)

### 2.1. Fundamentals

Consider two functions  $f(x, y)$  and  $g(x, y)$  over  $\mathbb{R}^2$  that are absolutely

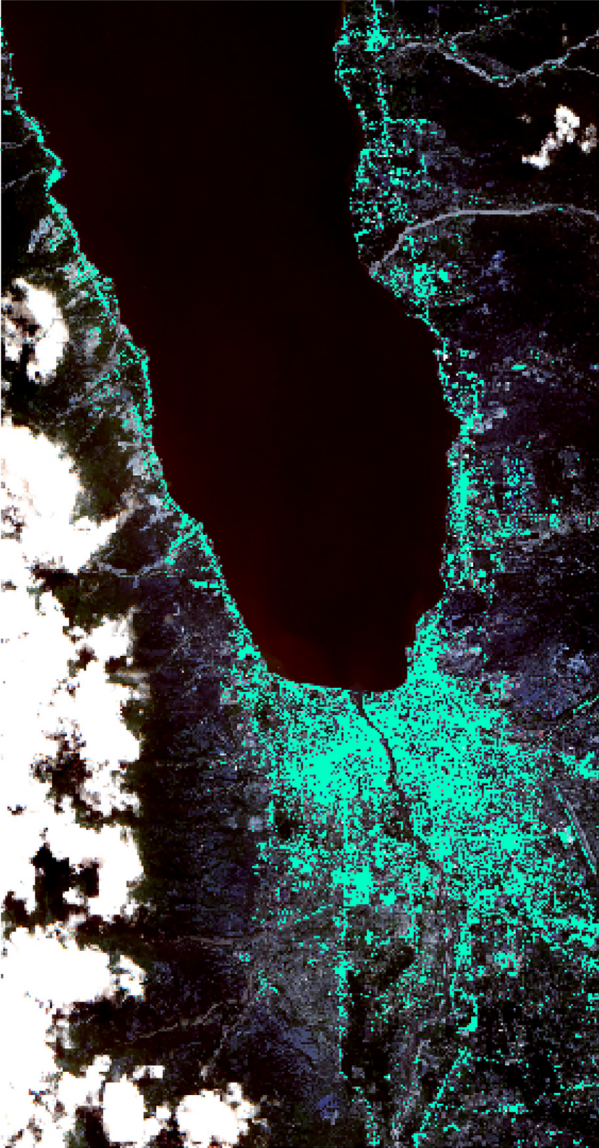


Fig. 6. Urban footprint over the study area shown in cyan. The urban footprint was estimated using a land cover classification from Sentinel-2 imagery. (For interpretation of the references to color in this figure legend, the reader is referred to the web version of this article.)

integrable and have the following relation:

$$g(x, y) = f(x - x_0, y - y_0) \quad (1)$$

Its equivalence in the frequency domain, due to the Fourier shift property, is:

$$G(u, v) = F(u, v)\exp(-j(ux_0 + vy_0)) \quad (2)$$

where  $F(u, v)$  and  $G(u, v)$  are the Fourier transforms of  $f(x, y)$  and  $g(x, y)$ , respectively. The normalized cross power spectrum is defined as

$$\begin{aligned} \hat{R}(u, v) &= \frac{F(u, v)\overline{G(u, v)}}{|F(u, v)G(u, v)|} \\ &= \exp(j(ux_0 + vy_0)) \end{aligned} \quad (3)$$

The inverse Fourier transform of  $\hat{R}$  results in the Dirac delta function centred at  $(-x_0, -y_0)$ ,  $\delta(x + x_0, y + y_0)$ . Image analysis deals with discrete domains, and thus, it is necessary to consider the different properties. Let us define the discrete domain as  $n_1 = -M_1, \dots, M_1$  and  $n_2 = -M_2, \dots, M_2$ . The functions  $f(n_1, n_2)$  and  $g(n_1, n_2)$  are defined as:

$$\begin{aligned} f(n_1, n_2) &= f(x, y)|_{x=n_1T_1, y=n_2T_2} \\ g(n_1, n_2) &= f(x - x_0T_1, y - y_0T_2)|_{x=n_1T_1, y=n_2T_2} \end{aligned} \quad (4)$$

where  $T_1$  and  $T_2$  are the spatial sampling intervals, that is, the pixel resolution. The expression equivalent to Eq. (3) in the discrete domain is

$$\hat{R}(u, v) = \frac{\hat{F}(u, v)\overline{\hat{G}(u, v)}}{|\hat{F}(u, v)\hat{G}(u, v)|} \quad (5)$$

where  $\hat{F}$  and  $\hat{G}$  denote the discrete Fourier transforms (DFTs) of  $f(n_1, n_2)$  and  $g(n_1, n_2)$ , respectively. The PC is the inverse discrete Fourier transform (IDFT) of  $\hat{R}$ ; thus, we can think of the PC as a bidimensional array or a matrix. If  $x_0$  and  $y_0$  are integer values, then the PC approximates a unit pulse. The component of the PC that contains the pulse is termed the *coherent component*. However, in real practice, the offset between images is often not a multiple of the pixel resolution (i.e., either  $x_0$  or  $y_0$  are not integers). Takita et al. (2013) used Eq. (2) as an approximation:

$$\hat{G}(k_1, k_2) \cong \hat{F}(k_1, k_2) \cdot \exp\left(-2j\pi\left(\frac{k_1x_0}{N_1} + \frac{k_2y_0}{N_2}\right)\right) \quad (6)$$

and approximated the PC in the following closed form:

$$\hat{r}(n_1, n_2) \cong \frac{\alpha}{N_1N_2} \frac{\sin \pi(n_1 + x_0)}{\sin \frac{\pi}{N_1}(n_1 + y_0)} \frac{\sin \pi(n_2 + x_0)}{\sin \frac{\pi}{N_2}(n_2 + y_0)} \quad (7)$$

To achieve subpixel image registration, Takita et al. (2013) proposed to first compute the inverse discrete Fourier transform (IDFT) of  $\hat{R}$  (Eq. (5)) and then to use the main peak and the components adjacent to it to estimate  $\alpha$ ,  $x_0$ , and  $y_0$  of Eq. (7) by using some function fitting procedure. Foroosh et al. (2002) defined a similar closed form of the PC;

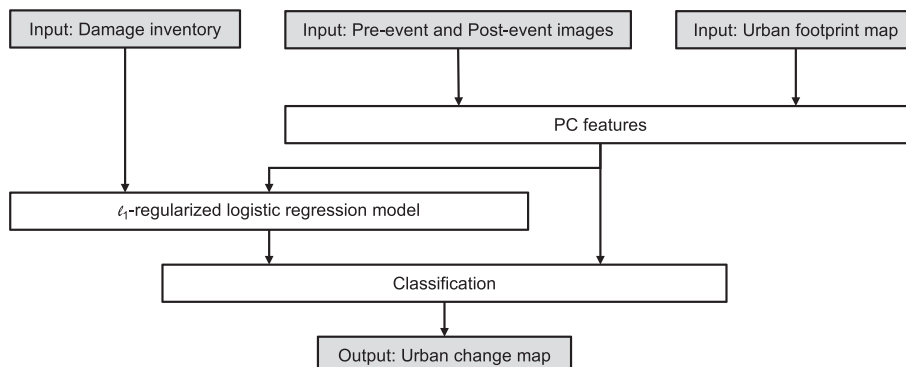
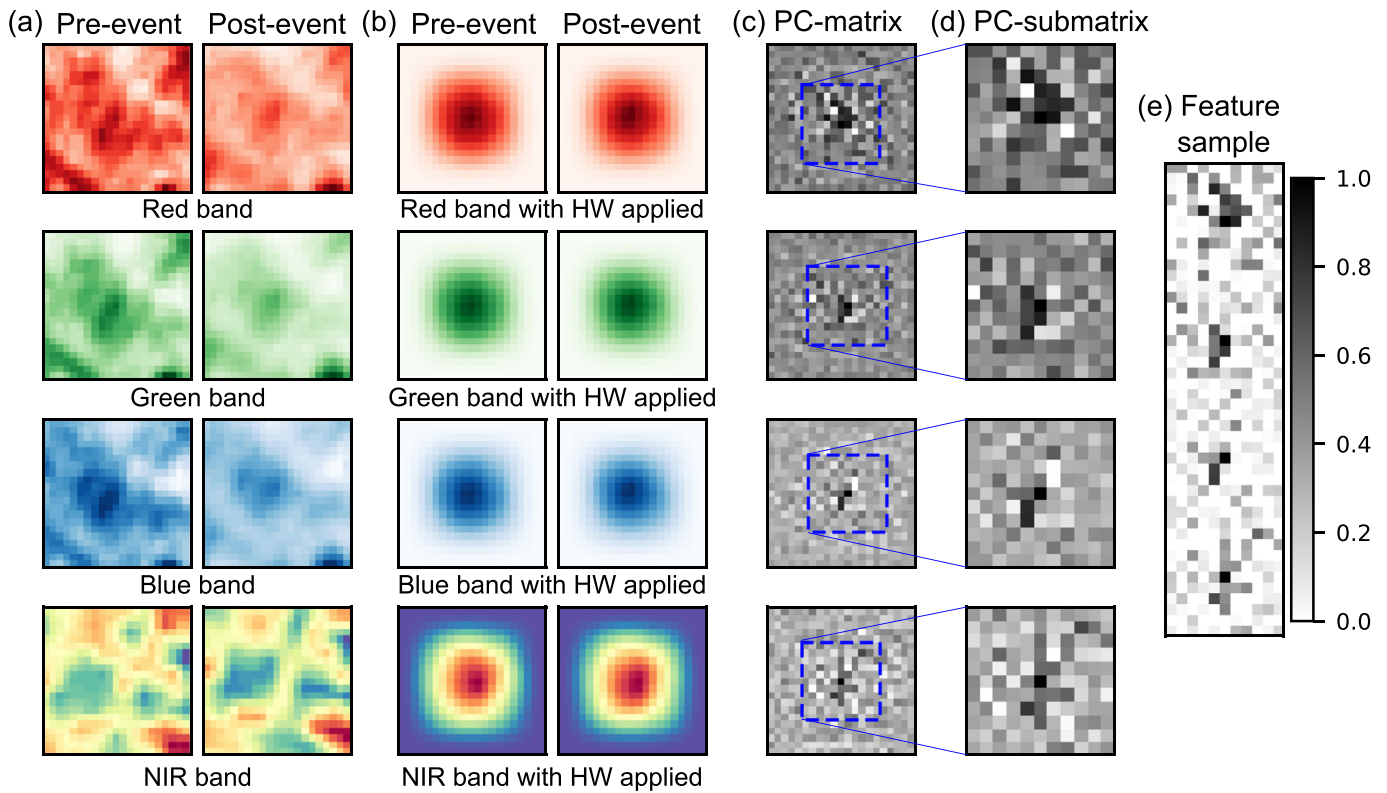
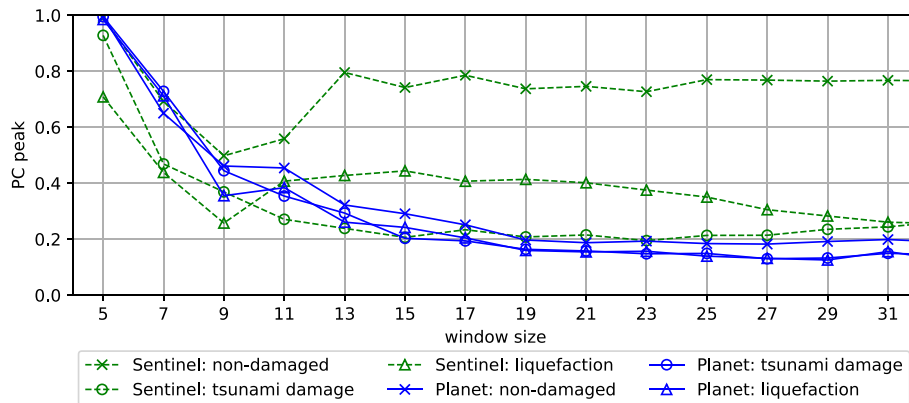


Fig. 7. Processing chain for urban change mapping.



**Fig. 8.** Construction of a feature sample matrix. (a) Image input. Each row represents a spectral band. The left and right columns denote the images acquired before and after the earthquake-tsunami, respectively. (b) Images with Hanning window (HW) applied. (c) Computation of the PC-matrix. (d) PC submatrix of size  $11 \times 11$  with the PC peak value in its center. (e) The feature sample matrix is constructed by merging the 4 PC-submatrices.



**Fig. 9.** Relationship of the PC peak value and the window size.

in their study, they assumed that the pixel resolution is an integer multiple of the subpixel offset. Under this assumption, [Foroosh et al. \(2002\)](#) provided a rigorous demonstration that more than one coherent component is present when either  $x_0$  or  $y_0$  are not integer values.

### 2.2. PC-based features for change detection

PC has remarkable properties compared to the classical cross correlation method. For instance, the coherent components of the PC form a distinctive sharp peak. Another suitable property is that the PC is invariant to uniform variations in the illumination and offsets in the average intensity; hence, the PC is robust to images acquired during different seasons and to fixed gain errors due to calibration. [Fig. 1](#) shows pairs of red-band optical images recorded by DigitalGlobe before and after the 2018 Sulawesi Indonesia earthquake-tsunami. Yellow

dashed grid lines are drawn to emphasize the offsets between the images. The PCs showed in [Fig. 1a](#) and [b](#) exhibit a clear peak. That is, the images are quite similar, and no significant changes are observed. On the other hand, the PC shown in [Fig. 1c](#) does not exhibit a prominent peak. There are significant changes between these images mainly because a building is non-damaged in one image, while it is collapsed in the other.

In this study, the PC-matrix is used to construct a feature space to identify changes in urban areas. For that purpose, the PC is shifted such that the peak value is centered. [Fig. 2](#) illustrates a closer look at a cross-section through the PC peak of the examples shown in [Fig. 1](#) after being aligned. Recall that the coherent components are of great relevance in the detection of changes. However, the number of coherent components is unknown. In fact, if the image exhibits non-linear distortions over the entire study area, the number of coherent components of the PC

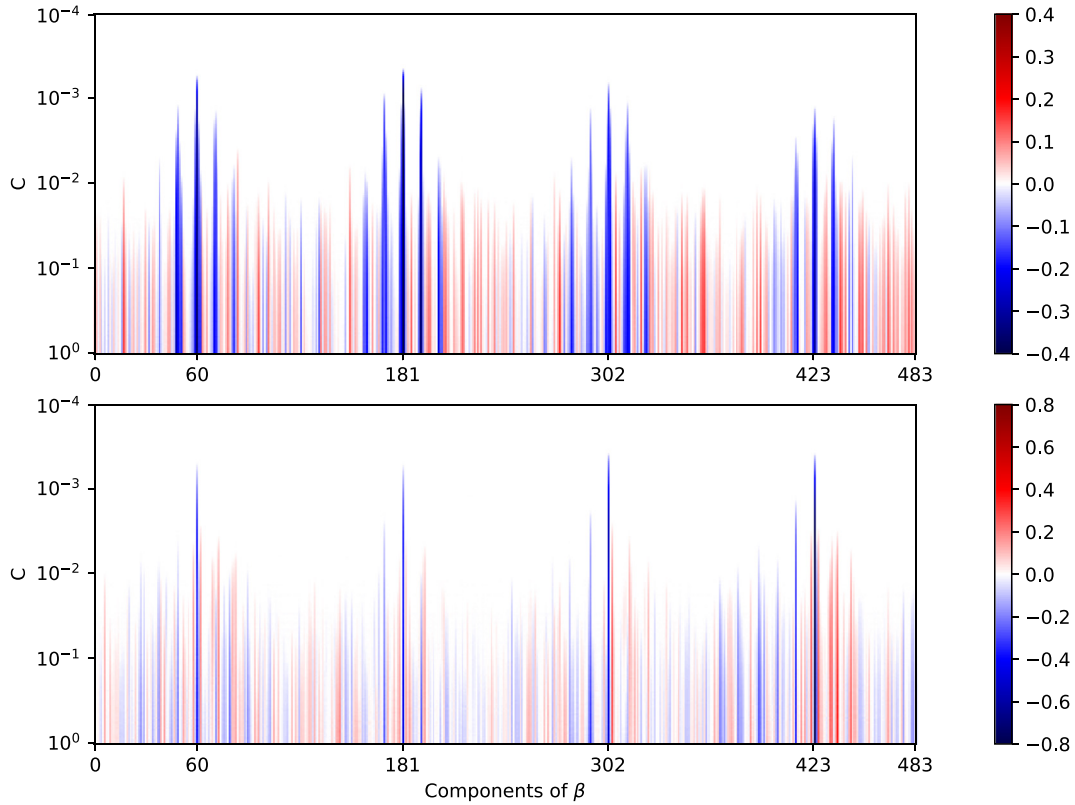


**Fig. 10.** Components of vector  $\beta$  calibrated from the  $\ell_1$ -regularized logistic regression classifier. Note that  $\beta$  consists of 484 components (x-axis). The vector  $\beta$  was computed under different values of the parameter  $C$  (y-axis). Top: Vector  $\beta$  calibrated from the feature space constructed from the Planet imagery. Bottom: Vector  $\beta$  calibrated from the feature space constructed from the Sentinel-2 imagery.

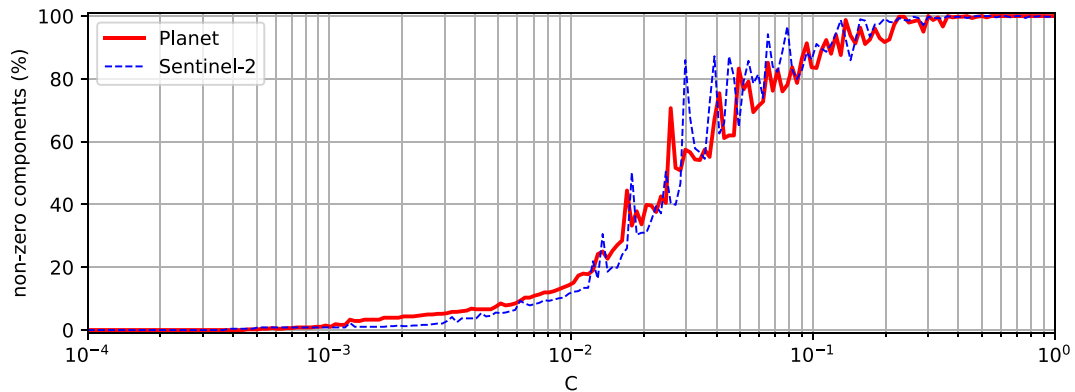


**Fig. 11.** Percentage of the non-zero components of vector  $\beta$  as a function of  $C$ . The red solid line denotes the results obtained from the feature space constructed from the Planet imagery and the blue dashed line denotes that obtained from the Sentinel-2 imagery. (For interpretation of the references to color in this figure legend, the reader is referred to the web version of this article.)

computed over a moving window differs from one zone to another. Moreover, based on previous studies, the number of coherent components certainly represents only a small number of the components of the PC-matrix. The next section introduces the strategy that will be followed to identify those components.

### 3. $\ell_1$ -Regularized logistic regression classifier

Consider a set of  $M$  samples  $(\mathbf{r}_i, z_i)_{i=1}^M$ , where  $\mathbf{r}_i \in \mathbb{R}^n$  is a feature vector and  $z_i \in \{-1, 1\}$  is an associated binary response. It is assumed that the vectors  $\mathbf{r}_i$  have been standardized such that  $\frac{1}{M} \sum_i \mathbf{r}_{ij} = 0$  and  $\frac{1}{M} \sum_i \mathbf{r}_{ij}^2 = 1$ , where  $\mathbf{r}_{ij}$  denotes the  $j$ th-component of a feature vector  $\mathbf{r}_i$ . This paper addresses binary discrimination, that is, whether an urban

area exhibits changes ( $z_i = 1$ ) or not ( $z_i = -1$ ). The conditional probability  $Pr(z_i = 1|\mathbf{r}_i)$  is defined as:

$$Pr(z_i = 1|\mathbf{r}_i) = \frac{\exp(\beta_0 + \beta^T \mathbf{r}_i)}{1 + \exp(\beta_0 + \beta^T \mathbf{r}_i)} \tag{8}$$

where  $\beta_0$  is an intercept term, and  $\beta \in \mathbb{R}^n$  is a vector of regression coefficients. Here, the approach to fit the logistic model is based on minimizing the negative log-likelihood with  $\ell_1$ -regularization:

$$\text{minimize}_{\beta_0, \beta} \left\{ -\frac{1}{M} \sum_{i=1}^M \log(1 + \exp(-z_i(\beta_0 + \beta^T \mathbf{r}_i))) + \lambda \|\beta\|_1 \right\} \tag{9}$$

where  $\|\cdot\|_1$  denotes the  $\ell_1$ -norm. Further details on Eq. (9) can be found in [Hastie et al. \(2015\)](#). As carefully explained in [Section 4.2.1](#),  $\mathbf{r}_i$

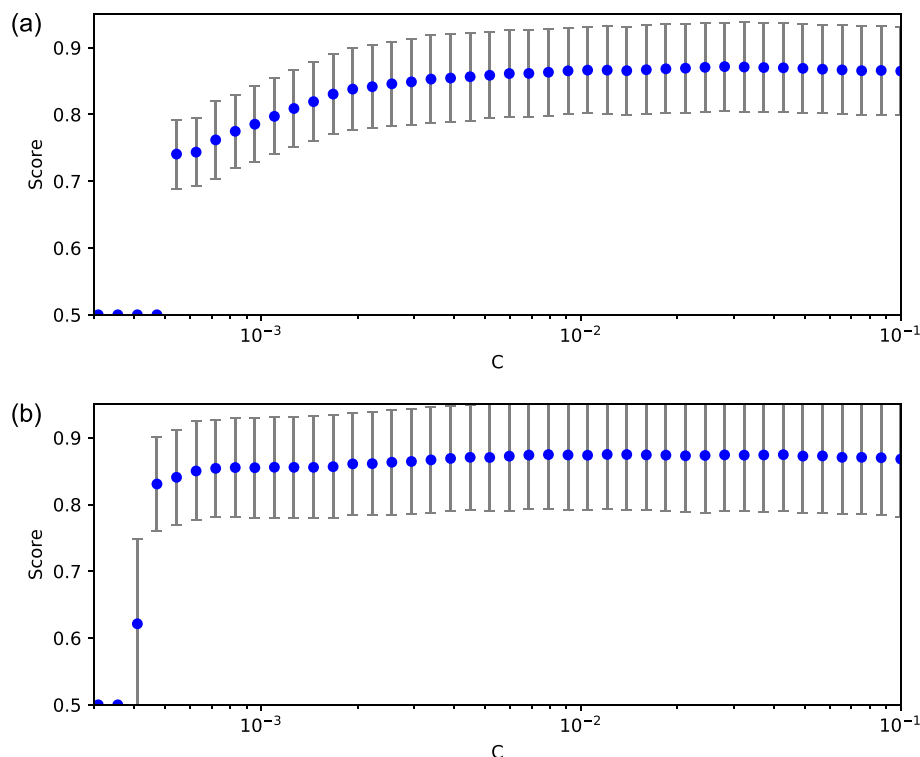


**Fig. 12.** Ten-fold cross-validation curves for the samples constructed from the Planet (top) and Sentinel-2 (bottom) imagery. The blue marks denote the averaged overall accuracy, and the gray bars denote the standard deviation error. (For interpretation of the references to color in this figure legend, the reader is referred to the web version of this article.)

represents the PC-matrices rearranged in a vector format. The term  $\lambda \|\beta\|_1$  is denoted as the  $\ell_1$ -penalty. The key property of the  $\ell_1$ -penalty is that it yields sparse solutions. A sparse solution refers to a solution in which the vector  $\beta$  has relatively few non-zero components, a property that will be exploited to identify the coherent components of the PC-matrix. The *sparse level*, defined here as the fraction of zero-valued components, increases as  $\lambda$  increases. The optimization problem is also expressed in the following form:

$$\underset{\beta_0, \beta}{\text{minimize}} \left\{ C \sum_{i=1}^N \log(1 + \exp(-z_i(\beta_0 + \beta^T \mathbf{r}_i))) + \|\beta\|_1 \right\} \quad (10)$$

Thus, the sparse level increases as  $C$  decreases, which is sometimes more convenient to assess vector  $\beta$  under different sparse levels. The utility of this modification will be shown in Chapter 4.

#### 4. Empirical evaluation: the 2018 Sulawesi Indonesia earthquake-tsunami

On September 28, 2018, an earthquake of Mw 7.5 occurred 75 km north of the city of Palu, Central Sulawesi, Indonesia. The epicenter was located in the northern part of Donggala District on an active strike-slip fault called Palu-Koro (Socquet et al., 2019). The earthquake induced a tsunami, whose mechanism remains controversial (Muhari et al., 2018; Arikawa et al., 2018; Heidarzadeh et al., 2019; Takagi et al., 2019; Sassa and Takagawa, 2019). Evidence from a field survey suggests that the maximum flow depth and tsunami height were 8 m and 10 m, respectively (Muhari et al., 2018). Furthermore, another effect was produced by this earthquake. The transient ground motion of the earthquake generated excess pore pressure within the undrained cohesionless soil. This phenomenon, well known as *liquefaction* (Kramer, 1996), compromised the shear strength of the soil and produced significant soil deformation, soil flow (that is, as a fluid), and lateral spreading. As a result, this earthquake, together with its secondary effects, resulted in an extensive damaged area. As of October 25, 2018, approximately 68,451 damaged houses, 2081 casualties, and 4438 injured people had been reported (The AHA Centre, 2018).

Because the Palu-Koro fault crosses directly through the city of Palu, the slip distribution (Bao et al., 2019; Socquet et al., 2019), soil liquefaction, and lateral spreading ultimately produced very complex ground deformation in many areas of the city. Fig. 3 shows a close-up of an urban area in Palu city recorded by DigitalGlobe (2018) before and after the earthquake. Liquefaction is observed in the bottom-left corner. The orange dashed line denotes the location of the fault line. Recall that this fault completely traverses the city of Palu. The yellow arrows denote estimates of the horizontal offset between the images. Note that the north-south component of the offset on the left side of the fault is opposite to that on the right side, which highlighted by the distortions of the roads and streets. Furthermore, the offset magnitude increases from south to north. Given these characteristics, it is evident that the earthquake was the main source of the offsets between the images. Fig. 4 shows the fault line crossing an agricultural field. Surface rupture is observed because the linear arrangement of the crops is perpendicular to the slip orientation. Deformation of 3.72 m was observed in the referred agricultural field. As a result, image registration is challenging to apply along the fault line and the areas that experienced liquefaction, and therefore, change detection-based damage identification must be conducted carefully. The use of PC-matrix is a good option for identifying damage in the infrastructure.

##### 4.1. Data used

Because of their ability to cover large areas, medium-resolution images are used in this study to detect urban changes between a pair of images taken before and after the 2018 Sulawesi Indonesia earthquake-tsunami. Three-meter resolution imagery provided by Planet (2018) and 10 m resolution imagery provided by Sentinel-2 are evaluated in independent experiments. Additional specifications of the images are shown in Table 1. The visible and near-infrared (VNIR) bands are used in both studies. Fig. 5a shows the location of the study area in the western part of Sulawesi, Indonesia, which covers around 475 km<sup>2</sup>. This study focuses on the city of Palu, the most severely affected zone, and its surroundings. Fig. 5b and c show the visible spectral bands of the satellite images acquired on September 28, 2018, and October 1, 2018,

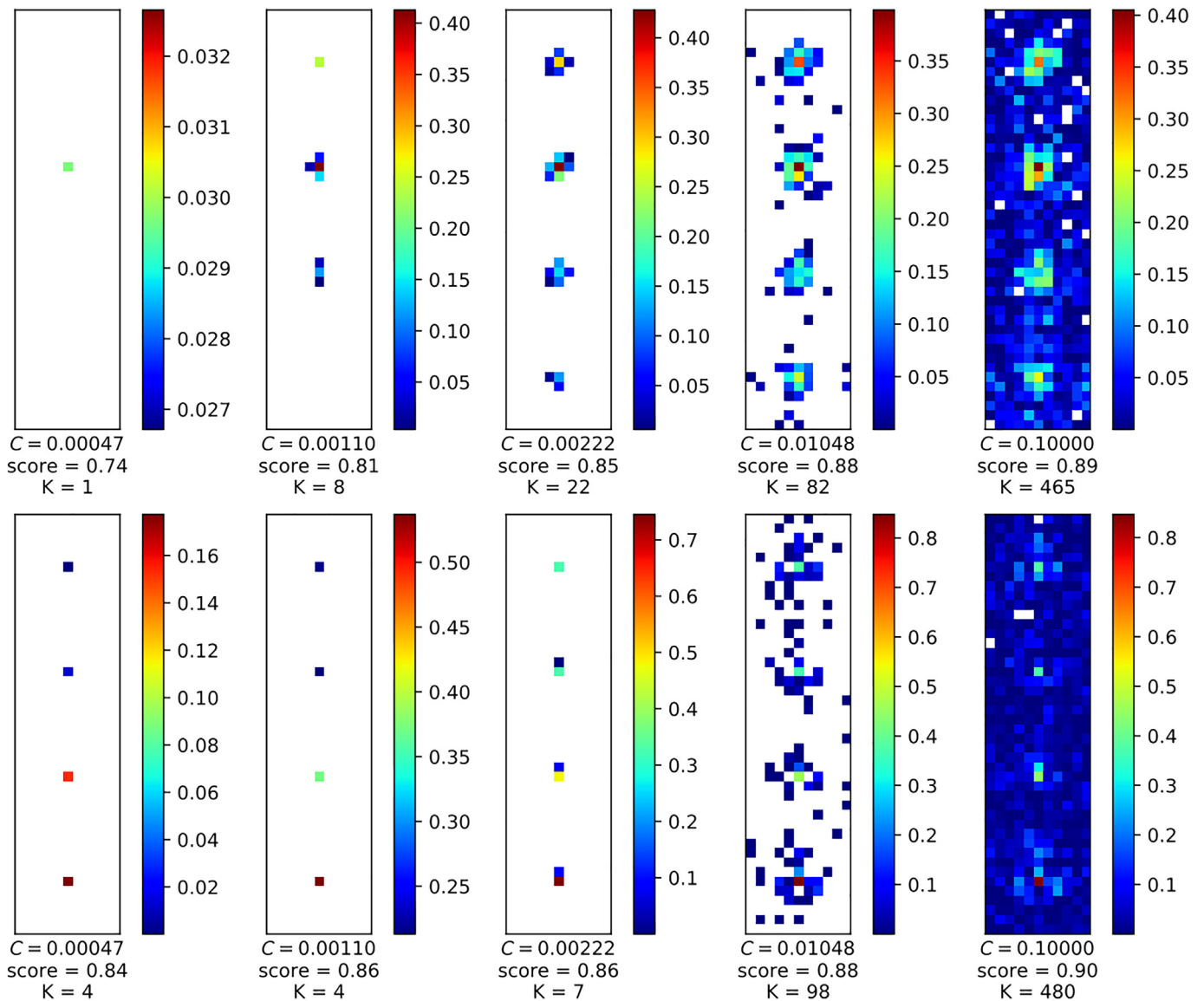


Fig. 13. Vector  $\beta$ , rearranged as a matrix in the same way as a feature sample matrix (Fig. 8e), computed from different values of  $C$ . Top: Results obtained from the Planet feature space. Bottom: Results obtained from the Sentinel-2 feature space. The  $K$ -value below each plot denotes the number of non-zero components of  $\beta$ .

by Planet (2018). Likewise, Fig. 5d and e shows the images acquired on August 18, 2018, and October 2, 2018, by Sentinel-2. Moreover, high-resolution (50-cm resolution) optical imagery recorded on October 2, 2018, by DigitalGlobe (2018) will be employed to assess the results.

To filter out vegetation areas that are sensitive to changes of types other than those produced by the earthquake or tsunami, a map that indicates only infrastructures is necessary. Hereafter, this map is referred to as an urban footprint map. A series of routines for generating samples automatically from multitemporal Sentinel-2 images were established. We used Sen2Cor (The European Space Agency, 2018) to perform atmospheric, terrain, and cirrus corrections on top-of-atmosphere radiance data (Level 1C) and generate bottom-of-atmosphere reflectance data (Level 2A). Scene classification maps generated by Sen2Cor via unsupervised techniques were used to select training samples of vegetation, soil, water, and clouds. We obtained training samples of artificial surfaces (i.e., urban areas) from OpenStreetMap layers of buildings and roads. Canonical correlation forest (Rainforth and Wood, 2015) that extends random forest with canonical correlation-based feature extraction was adopted as a classifier. A total of eleven Sentinel-2 datasets acquired in 2018 before the event were processed, and the final classification map was created by the majority

voting of multi-temporal land cover maps. The resulting product, which has a ground sampling distance of 10 m, is shown in Fig. 6.

The following describes the database used to calibrate and test the  $\ell_1$ -regularized logistic regression classifier. Copernicus, Emergency Management Service (2018) provided a building damage inventory. The damage condition was evaluated through visual interpretation of the entire affected area with post-event optical satellite imagery with a 50-cm resolution. The first report of the complete survey was released approximately one week after the earthquake-tsunami, and updated versions were released on subsequent days. Four damage grades were defined: destroyed, damaged, possibly damaged, and non-damaged. Additionally, on October 20–22, 2018, the fourth author led a field investigation as part of the Indonesian government's reconnaissance (Koshimura et al., 2019). The survey aimed to measure the extent of tsunami inland penetration with RTK-GNSS (Fig. 15), to measure the flow depths, and to inspect structural damage. The surveyed area consisted of the middle-south area of Palu Bay. Buildings classified as destroyed and non-damaged by Copernicus agreed with observations performed during the field survey of Koshimura et al. (2019). On the other hand, buildings labeled as damaged and possibly damaged were controversial. Overall, the area inspected by Copernicus was much

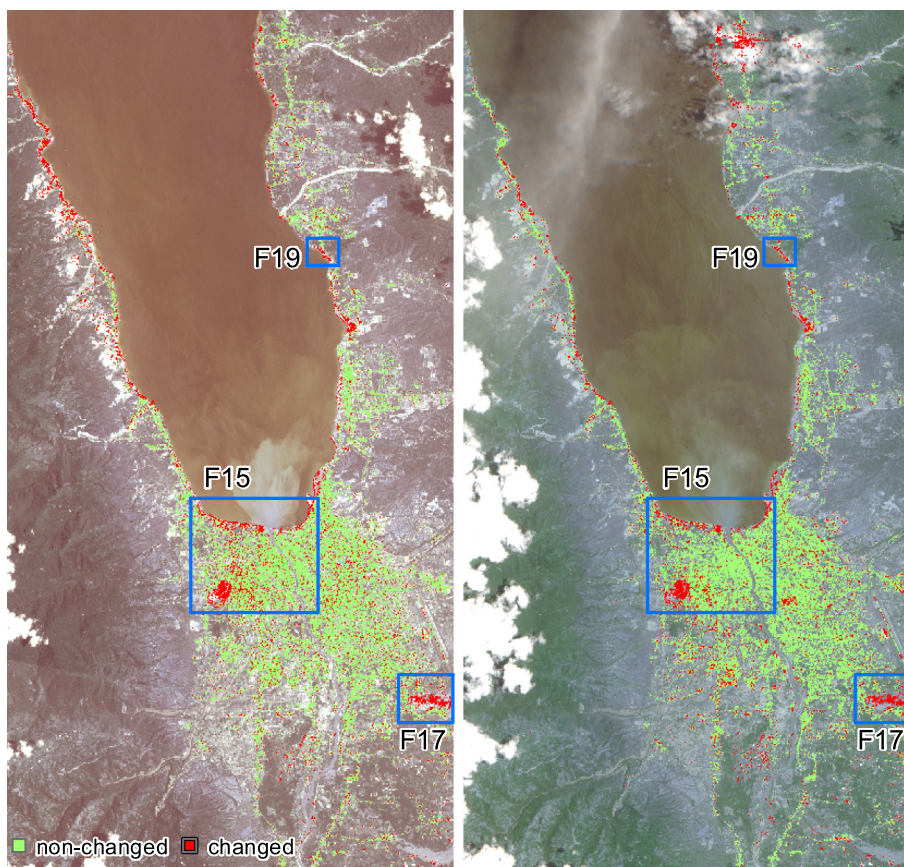


Fig. 14. Map with changes observed in the urban footprint areas computed from the Planet (left) and Sentinel-2 (right) imagery. The maps are shown on top of the post-event imagery used for the classification. The maps were computed using sparse models with  $C=0.0022$  for the Planet imagery and  $C=0.001$  for the Sentinel-2 imagery. Red and green pixels denote changed and non-changed urban areas, respectively, with a resolution of  $10 \times 10m^2$ . The rectangular boxes labeled F15, F17, and F19 denote the areas shown in Figs. 15, 17, and 19, respectively. (For interpretation of the references to color in this figure legend, the reader is referred to the web version of this article.)

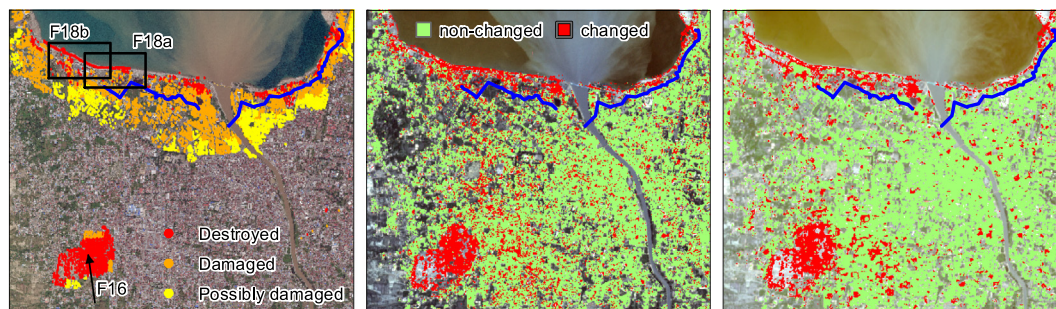


Fig. 15. A closer look at the central area of Palu Bay. The location of the area is shown in Fig. 14. Left: Damage inventory performed by Copernicus. Center: Changes detected from the Planet imagery. Right: Changes detected from the Sentinel-2 imagery. The blue line denotes the limits of the inundated area due to the tsunami traced by RTK-GNSS. The large changed area detected at the bottom left is one of the largest areas that experienced soil liquefaction. The black arrow labeled F16 denotes the orientation from which the photo shown in Fig. 16 was shot. The black rectangles labeled F18a and F18b denote the areas shown in Fig. 18a and b, respectively. (For interpretation of the references to color in this figure legend, the reader is referred to the web version of this article.)

more extensive than those surveyed by Koshimura et al. (2019). Besides, the identification of intermediate damage levels from medium resolution satellite images is doubtful. Therefore, in this study, samples labeled by Copernicus as damaged, possibly damaged, and non-damaged are merged as *non-changed*; whereas, samples labeled as destroyed are labeled as *changed*.

#### 4.2. Results

The block diagram in Fig. 7 shows the implemented processing chain. Three types of inputs are required: (i) The damage inventory, (ii) the pre- and post-event images, and (iii) the urban footprint map. First, the pre- and post-event images are used to compute the PC-matrices in urban areas and use them as input features. Then, the damage inventory is used to assign label class to some features samples and use them as

training input to calibrate the  $l_1$ -regularized logistic regression. Finally, a classification task is performed over the urban footprint map using the input features and the  $l_1$ -regularized logistic regression classifier. The final output is a map that indicates the damage-based changes in the urban areas. The performance of the proposed procedure was evaluated separately on both the imagery recorded by Planet and the imagery recorded by Sentinel-2. In the following, more details of every stage are provided.

##### 4.2.1. PC features

The construction of the feature space for the Planet imagery is summarized in Fig. 8. The PC is computed from the pre- and post-event images for each spectral band. A moving window of  $21 \times 21$  pixels is used. First, because Fourier analysis assumes periodicity, a 2D Hanning window is applied to each sub-image. Then, the PC-matrix is computed,



Fig. 16. A survey photo taken by Koshimura et al. (2019) in the urban area that experienced soil liquefaction. Its location is shown in Fig. 15.

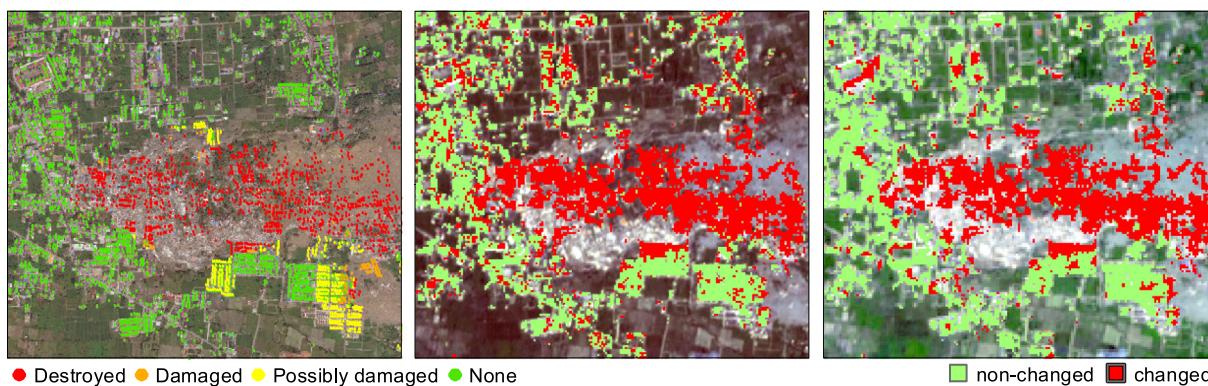


Fig. 17. Wide liquefaction area induced by the 2018 Indonesia earthquake-tsunami. Left: Damage survey performed by Copernicus. Center: Changes detected using the Planet imagery. Right: Changes detected using the Sentinel-2 imagery. The location of this area is shown in Fig. 14.

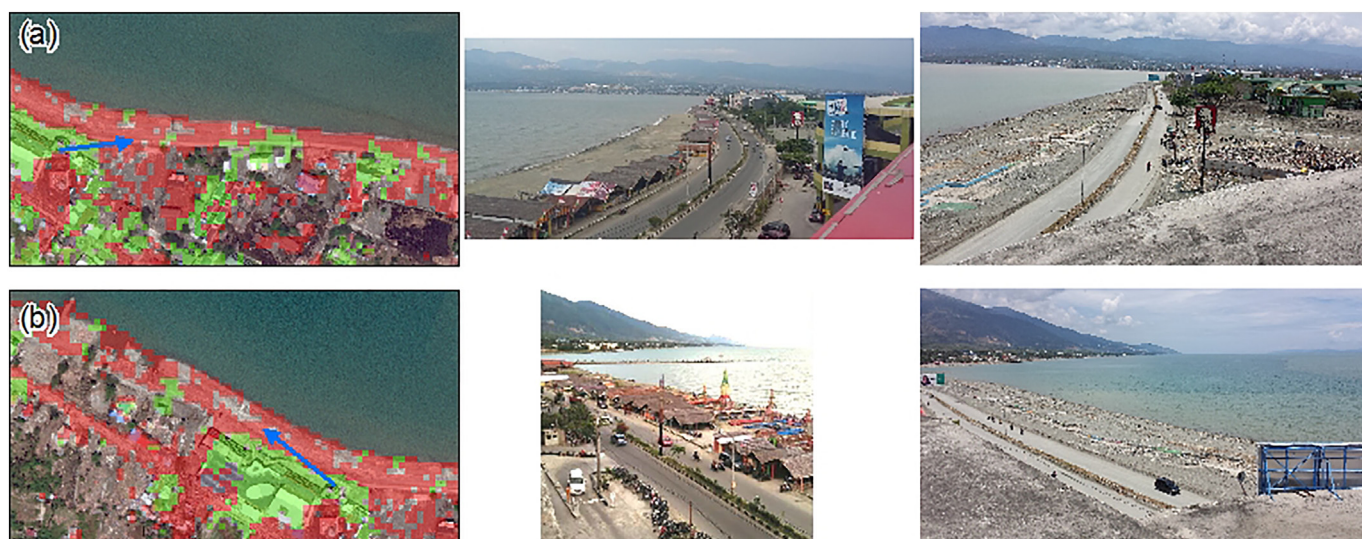
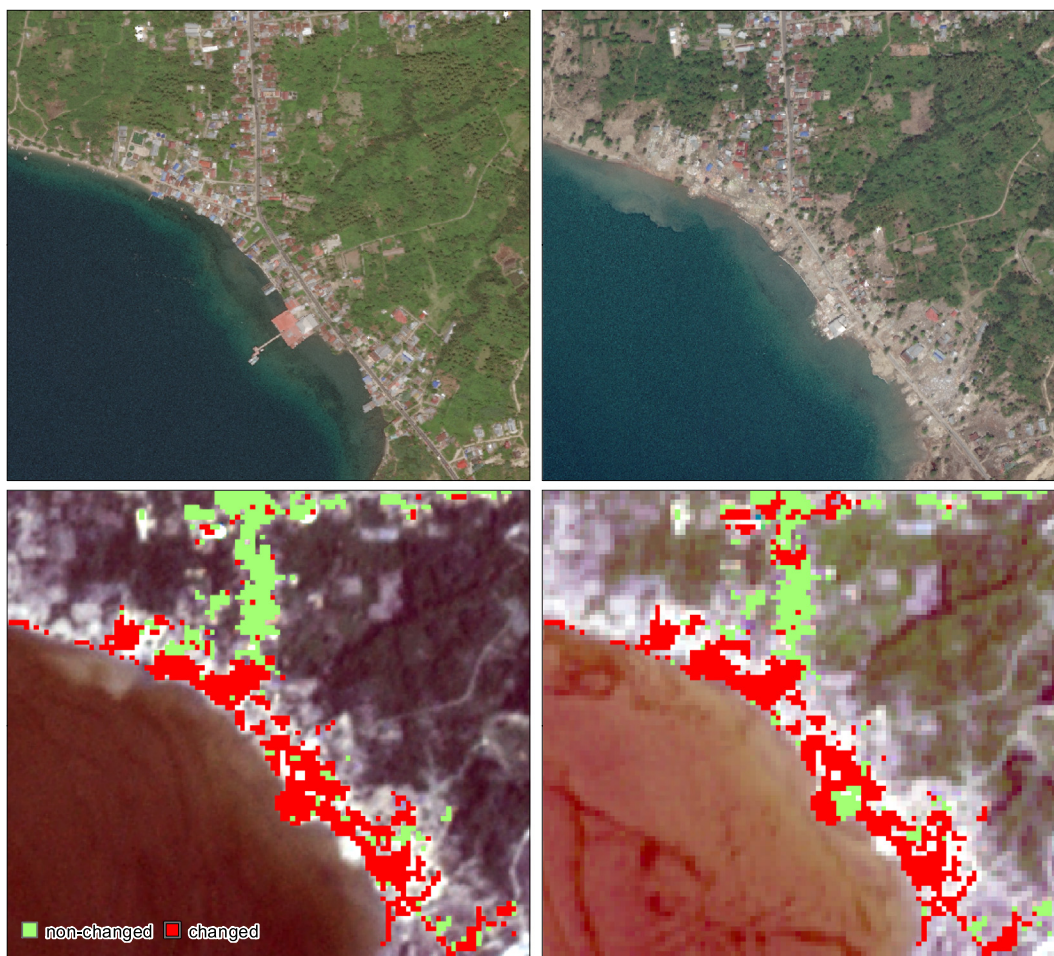


Fig. 18. Closer look at the estimated damage in the center of Palu Bay. The locations of the areas are shown in Fig. 15. Left: High-resolution optical imagery provided by DigitalGlobe overlaid with the changes detected from the Sentinel-2 imagery. The red areas are the detected changes in the urban areas, whereas the areas colored green are non-changed urban areas. Center: Photos taken before the tsunami and posted on Google Maps. Right: Photos taken by Koshimura et al. (2019) after the earthquake-tsunami. The blue arrows shown in the left column represent the directions from which the photos were shot. (For interpretation of the references to color in this figure legend, the reader is referred to the web version of this article.)



**Fig. 19.** Changes detected over the tsunami inundation area. Top: High-resolution optical images taken before (left) and after (right) the earthquake-tsunami. The images were provided by DigitalGlobe. Bottom: Changes detected over the urban footprint map computed from the Planet imagery (left) and the Sentinel-2 imagery (right). The location of this area is shown in Fig. 14.

**Table 2**

Comparison of  $\ell_1$ -regularized logistic regression with other three classifiers:  $\ell_2$ -regularized logistic regression, support vector machine with linear function kernel (SVM-linear), and support vector machine with radial basis function kernel (SVM-rbf). LR: logistic regression.

Classifier	Score (%)	Runtime (s)
$\ell_1$ -Regularized LR	85 $\pm$ 6	30
$\ell_2$ -Regularized LR	86 $\pm$ 7	38
SVM-linear	86 $\pm$ 7	1049
SVM-rbf	89 $\pm$ 6	239

and an  $11 \times 11$  submatrix is stored. The PC-submatrix contains the PC peak in its center. Then, a feature sample matrix is defined here as the four PC-submatrices merged, as depicted in Fig. 8e. Lastly, the feature vector,  $\mathbf{r}_i$ , defined in Section 3, is the feature sample matrix rearranged as a vector. Note that each PC-submatrix contributes with  $11 \times 11 = 121$  features to the feature space. Thus, the dimension of  $\mathbf{r}_i$  is 484. A similar procedure was applied to construct the feature space from the Sentinel imagery using a moving window of  $11 \times 11$  pixels, and the PC's maximum value was centered by applying a circular shift.

Regarding the selection of the window size, it was determined from a small, but a representative number of samples of non-changed, and tsunami/liquefaction-based changed areas. Fig. 9 depicts the PC peak value computed under different window sizes. Note that the smallest window size exhibits the largest PC peak. Then, as the window size increases, the PC peak quickly decreases until it reaches the window

size of  $9 \times 9$  for Sentinel-1 imagery and about  $19 \times 19$  for Planet imagery. The largest correlation observed in the window size of  $5 \times 5$  is mainly because the Hanning window applied to both images before PC was computed. Thus, in this study, we used a window size of  $11 \times 11$  and  $21 \times 21$  for Sentinel-1 and Planet imagery, respectively. Recall that a larger window size shows a higher correlation peak for the non-changed areas but at the expenses of spatial resolution. An additional factor that needs to be considered is that the maximum measurable shift between the images must be lower than the window size. Based on the sampling theorem, the minimum window size must be twice the maximum measurable shift; however, most of the previous studies used bigger window sizes.

#### 4.2.2. Calibration of the $\ell_1$ -regularized logistic regression

Feature samples were computed at the location of Copernicus's survey and used to calibrate the  $\ell_1$ -regularized logistic regression classifier. A total of 8558 samples from the Copernicus survey were used as ground truth data for training and testing; 50% of the samples consisted of destroyed buildings, and the other 50% consisted of non-damaged buildings. The discriminant function was calibrated several times using Eq. (10) over a range of values for the parameter  $C$ . Fig. 10 depicts the effect of  $C$  over the vector  $\beta$  and Fig. 11 shows the relation of  $C$  and the number of non-zero components of  $\beta$ . Note that less than 5% of the components of  $\beta$  are non-zero when  $C$  is less than  $10^{-3}$ , and less 20% when  $C$  is less than  $10^{-2}$ . Furthermore, almost every component is non-zero when  $C > 0.3$ . These patterns are observed from both the results from Planet and the results from Sentinel-2 imagery (Fig. 11).

The 10-fold cross-validation was applied to evaluate the performance of the  $\ell_1$ -regularized logistic regression. That is, the ground truth data are randomly divided into 10 subsets, from which 9 subsets are used for calibration, and the remaining subset is used to evaluate the accuracy. The fraction of correctly classified samples, termed the *overall accuracy*, is employed as a score for the evaluation. This process is repeated 10 times, each with a different subset for the accuracy evaluation. The 10-fold cross-validation was applied for different values of  $C$  over the two experiments, and the results are reported in Fig. 12. The blue mark denotes the averaged score, and the bars denote the limits of the average plus/minus the standard deviation. Note that the score is 50% in the lowest value of  $C$ . This situation occurs when the components of  $\beta$  are all zero. The accuracy is 50% because the ground truth data are balanced (that is, the same amount of samples exist for each class), and all the testing data are classified as the same class. For the Planet imagery, once  $\beta$  obtains its first non-zero component (see the top of Fig. 10) at  $C \approx 0.0005$ , the classifier reaches an average performance of 75%. As  $C$  increases, the accuracy increases until it reaches an average score of about 85% at  $C \approx 0.003$ . Note that the standard deviation also increases slightly as  $C$  increases. The 10-fold cross-validation results computed from the Sentinel-2 samples show approximately the same maximum average score. However, the maximum performance is reached at a lower value of  $C$  than that from the Planet dataset.

Figs. 10–12 demonstrate that only a few non-zero components of vector  $\beta$  are necessary to achieve high accuracy. Fig. 13 provides a closer look at the coefficients of  $\beta$ , rearranged as a matrix in the same way as a feature sample matrix (Fig. 8e), under specific values of  $C$ . Note that as  $C$  increases from zero, the first non-zero component of  $\beta$  are those associated with the shape of the PC-peaks computed over the four bands. For the case of the Planet imagery, only these components of  $\beta$  are necessary to reach their maximum performance. These results suggest that the components adjacent to the PC peak are important as well, as can be confirmed with the results obtained with  $C=0.0022$ , from which only 22 components out of 484 were necessary to achieve the 85% accuracy (Fig. 13). Moreover, notice that higher values of  $C$  do not increase the accuracy significantly. Different behavior is observed in the case of Sentinel-2 imagery. Here, only the PC peaks are necessary to reach the maximum performance, 85% accuracy. In other words, additional components adjacent to the PC peak do not increase the accuracy.

#### 4.2.3. Urban change map

Fig. 14 shows the resulting changes detected over the urban footprint map (Fig. 6) computed from the Planet and Sentinel-2 imagery. The results from the Planet imagery were computed using a sparse model with  $C=0.0022$ , while those from the Sentinel-2 imagery were computed from a sparse model using  $C=0.001$ . In general, both results are consistent but with some differences in the northern area. One cause of these differences is the presence of clouds in the northeastern area of the post-event Sentinel-2 image, which produced false detections. Unfortunately, the differences between both maps in the northwestern area could not be carefully analyzed due to the low resolution of the images and the lack of additional information. A closer look at the central area of Palu Bay is depicted in Fig. 15. The results from the Planet imagery are noisier than those from the Sentinel-2 imagery. However, most of the changes detected in the urban footprint areas contain the buildings labeled as destroyed by Copernicus. The significant amount of detected changes in the bottom-left area of Fig. 15 represents the damage produced by soil liquefaction, which produced immense damage (see Fig. 16). Another wide area that experienced soil liquefaction is shown in Fig. 17. Regarding the damage produced by the tsunami, most of the changes detected along the central part of Palu Bay are located within the inundated area traced by RTK-GNSS (blue line in Fig. 15). Fig. 18 shows photos taken before and after the tsunami at the Palu Bay. Another tsunami-inundated area that was not surveyed by Copernicus but was detected from our results is depicted in Fig. 19. The

results were confirmed with high-resolution optical images provided by DigitalGlobe.

## 5. Discussion

Some issues require additional comments. For instance, the feature space used in this study consists of the fusion of four PC submatrices computed separately over four pairs of spectral bands (red, green, blue, and near-infrared bands, see Fig. 8). Each PC was computed by the application of a 2D Fourier transform, as detailed in Section 2. This is not the only way to construct a feature space. If hyperspectral images are available, 3D Fourier transform can be used directly instead of 2D Fourier transform applied to each spectral band. This potential method for constructing a feature space needs further evaluation and will constitute the subject of future studies.

For the sparse model, the lowest numbers of non-zero components of vector  $\beta$  to achieve an 85% overall accuracy were different for the two experiments. We believe the size of the offset with respect to the image resolution plays an important role in this matter. As shown in Fig. 3, the displacement is on the same order of magnitude as the pixel resolution (that is, 3 m) of the Planet imagery. On the other hand, the Sentinel-2 resolution, 10 m, is much larger. In order to confirm this hypothesis, it is necessary to conduct a study to observe the effect of the offset-image resolution relationship on the number of non-zero components of  $\beta$ . This task can be performed by applying synthetic offsets to the post-event image. It is worth noting that only a few components of the PC array are relevant, and thus, it is computationally efficient. Based on the observed results, we suggest using only 9 components per PC-matrix,  $3 \times 3$  with the PC peak centered, for change detection purposes.

One of the reasons that the resulting products exhibit some level of noise is because the proposed method detected changes in urban areas caused by factors other than the 2018 Sulawesi Indonesia earthquake-tsunami. Among these factors are (i) buildings constructed between the acquisition dates of the pre- and post-event images, (ii) increments in the numbers of human-made objects, such as the number of planes at an airport and the number of shelters established for the distribution of relief supplies, (iii) presence of vegetation within the urban areas. Another important factor for the misclassifications might be related to the noise and aliasing effect on the PC.

In terms of accuracy, the  $\ell_1$ -regularized logistic regression performs the same level of accuracy as other supervised machine learning classifiers. Table 2 reports the comparison of  $\ell_1$ -regularized logistic regression with  $\ell_2$ -regularized logistic regression, the support vector machine (SVM) with a linear function kernel, and the SVM with radial basis function (rbf) kernel. The runtime used to perform the 10-fold cross-validation is reported as well. As can be observed, all the classifiers exhibit similar levels of accuracy. The SVM with rbf kernel shows the highest score. It might be because it uses a non-linear discriminant function. The advantage of the  $\ell_1$ -regularized logistic regression is the interpretation of the fitted model without sacrificing accuracy. Recall, the calibrated  $\ell_1$ -regularized logistic regression uses only 22 out of the 484 features computed from Planet imagery, whereas the other classifiers use the complete set of features. Thus, another advantage is the computational efficiency when predictions are performed.

In this study, we evaluate the use of the shape of the PC-peak as feature input to detect damage-based changes between a pair of images. It was assumed that the presence of the PC-peak is invariant with respect to translations in areas without changes. There are, however, other options. For instance, the Fourier-Mellin transformation can be used as invariant with respect to translation, rotation, and scale (Tong et al., 2019). The Fourier-Mellin transformation could be the right choice when the images have different orientations. It is worth noting, however, that it is customary to select the pre- and post-event images with similar acquisition conditions. After a large scale disaster, images are recorded at the earliest possible. Then, for the change detection

analysis, the closest pre-event image with similar acquisition conditions is selected from the archives. Thus, under this common practice, the effect of rotation and scale can be neglected.

## 6. Conclusions

In this study, the phase correlation (PC) was employed as a feature space to identify changes between a pair of images that are not co-registered. This research aims to identify changes produced by large-magnitude earthquakes that produce complex ground deformation patterns; thus, traditional image registration methods cannot precisely align such images. The fundamental principle of the use of PC is that it will show a prominent peak in areas that do not exhibit changes, whereas no peak is observed in areas that experience significant changes. Thus, we used a sparse logistic regression model to identify the relevant information from the PC. Moreover, we evaluated the performance of the proposed procedure on the detection of changes produced by the 2018 Sulawesi Indonesia earthquake-tsunami. For this purpose, the experiment was performed twice using visual and near-infrared (VNIR) spectral bands at different resolutions. In the first experiment, VNIR imagery with a 3-m pixel resolution provided by Planet was used. The second experiment used VNIR imagery with a 10-m pixel resolution provided by Sentinel-2.

Ground truth data provided by a third party were used for the calibration and testing of the  $l_1$ -regularized logistic regression classifier. The 10-fold cross-validation was performed, and an averaged overall accuracy of 85% was achieved in both experiments. From the feature space constructed from the Planet imagery, only 22 features out of 484 were necessary to achieve its maximum performance. Likewise, from the sample space constructed from the Sentinel-2 imagery, only 4 features were necessary to achieve its best performance. These results confirm that it is possible to detect changes in urban footprint maps between images that are not co-registered. Though this research was conceived to overcome the poor performance of traditional image registration in areas of complex ground deformation due to large-magnitude earthquakes, avoiding the image registration process might speed up the overall process of damage detection, which is also appealing in the context of early disaster response.

## CRedit authorship contribution statement

**Luis Moya:** Conceptualization, Methodology, Validation, Formal analysis, Investigation, Writing - original draft, Writing - review & editing, Visualization. **Abdul Muhari:** Investigation, Resources. **Bruno Adriano:** Conceptualization, Investigation, Software. **Shunichi Koshimura:** Investigation, Supervision, Project administration, Funding acquisition. **Erick Mas:** Investigation, Supervision, Writing - original draft. **Luis R. Marval-Perez:** Conceptualization, Methodology, Writing - original draft. **Naoto Yokoya:** Formal analysis, Software, Writing - original draft.

## Declaration of competing interest

The authors declare that they have no known competing financial interests or personal relationships that could have appeared to influence the work reported in this paper.

## Acknowledgment

This study was partly funded by the Japan Science and Technology Agency (JST) J-Rapid project number JPMJRR1803; the JST CREST project number JP-MJCR1411; the Japan Society for the Promotion of Science (JSPS) Kakenhi Program (17H06108); the Core Research Cluster of Disaster Science at Tohoku University, Japan (a Designated National University); and the National Fund for Scientific, Technological and Technological Innovation Development (Fondecyt -

Peru) within the framework of the “Project for the Improvement and Extension of the Services of the National System of Science, Technology and Technological Innovation” [contract number 038-2019]. The satellite images were preprocessed with ArcGIS 10.6 and ENVI 5.5, and the other processing and analysis steps were implemented in Python using GDAL and NumPy libraries.

## References

- Adriano, B., Mas, E., Koshimura, S., Sep. 2015. Buildings damage due to the 2013 haiyan typhoon inferred from Sar intensity images. In: 2015 IEEE 5th Asia-Pacific Conference on Synthetic Aperture Radar (AP SAR), pp. 667–671.
- Arikawa, T., Muhari, A., Okumura, Y., Dohi, Y., Afriyanto, B., Sujatmiko, K.A., Imamura, F., 2018. Coastal subsidence induced several tsunamis during the 2018 Sulawesi earthquake. *Journal of Disaster Research* sc20181204.
- Bai, Y., Gao, C., Singh, S., Koch, M., Adriano, B., Mas, E., Koshimura, S., Jan 2018. A framework of rapid regional tsunami damage recognition from post-event terrasar-x imagery using deep neural networks. *IEEE Geosci. Remote Sens. Lett.* 15 (1), 43–47.
- Bao, H., Ampuero, J.-P., Meng, L., Fielding, E.J., Liang, C., Milliner, C.W.D., Feng, T., Huang, H., 2019. Early and persistent supershear rupture of the 2018 magnitude 7.5 Palu earthquake. *Nat. Geosci.* 12, 200–205.
- Canty, M., 2014. *Image Analysis, Classification and Change Detection in Remote Sensing: With Algorithms for ENVI/IDL and Python*, Third edition. Taylor & Francis.
- Cole-Rhodes, A.A., Johnson, K.L., LeMoigne, J., Zavorin, I., Dec 2003. Multiresolution registration of remote sensing imagery by optimization of mutual information using a stochastic gradient. *IEEE Trans. Image Process.* 12 (12), 1495–1511.
- Copernicus, Emergency Management Service, 2018. EMSR317: Earthquake in Indonesia. available at <https://emergency.copernicus.eu/mapping/list-of-components/EMSR317> (Online; accessed 29-March-2019).
- DigitalGlobe, 2018. Indonesia Earthquake and Tsunami. available at <https://www.digitalglobe.com/ecosystem/open-data/indonesia-earthquake-tsunami> (Online; last accessed 06-June-2019).
- Fang, L., Xu, Y., Yao, W., Stilla, U., 2016. Estimation of glacier surface motion by robust phase correlation and point like features of Sar intensity images. *ISPRS J. Photogramm. Remote Sens.* 121, 92–112.
- Feng, R., Du, Q., Li, X., Shen, H., 2019. Robust registration for remote sensing images by combining and localizing feature- and area-based methods. *ISPRS J. Photogramm. Remote Sens.* 151, 15–26.
- Foroosh, H., Zerubia, J.B., Berthod, M., March 2002. Extension of phase correlation to subpixel registration. *IEEE Trans. Image Process.* 11 (3), 188–200.
- Ghosh, S., Huyck, C.K., Greene, M., Gill, S.P., Bevington, J., Svekla, W., DesRoches, R., Eguchi, R.T., 2011. Crowdsourcing for rapid damage assessment: the global earth observation catastrophe assessment network (geo-can). *Earthquake Spectra* 27 (S1), S179–S198.
- Gokon, H., Koshimura, S., Matsuoka, M., 2016. Object-based method for estimating tsunami-induced damage using terrasar-x data. *Journal of Disaster Research* 11 (2), 225–235.
- Goncalves, H., Goncalves, J.A., Corte-Real, L., March 2011. Hairis: a method for automatic image registration through histogram-based image segmentation. *IEEE Trans. Image Process.* 20 (3), 776–789.
- Hastie, T., Tibshirani, R., Wainwright, M., 2015. *Statistical Learning With Sparsity: The Lasso and Generalizations*. Chapman & Hall/CRC.
- Heidarzadeh, M., Muhari, A., Wijanarto, A.B., Jan 2019. Insights on the source of the 28 september 2018 Sulawesi tsunami, Indonesia based on spectral analyses and numerical simulations. *Pure Appl. Geophys.* 176 (1), 25–43.
- Karimzadeh, S., Matsuoka, M., 2017. Building damage assessment using multisensor dual-polarized synthetic aperture radar data for the 2016 m 6.2 amatrice earthquake, Italy. *Remote Sens.* 9 (4).
- Kern, J.P., Pattichis, M.S., May 2007. Robust multispectral image registration using mutual-information models. *IEEE Trans. Geosci. Remote Sens.* 45 (5), 1494–1505.
- Koshimura, S., Muhari, A., Adriano, B., Moya, L., Ayunda, D., Afriyanto, B., Mas, E., April 2019. Field survey of the 28 september earthquake tsunami of Sulawesi, Indonesia. In: EGU General Assembly. *Geophysical Research Abstracts* 21 (Vienna, Austria).
- Kramer, S.L., 1996. *Geotechnical Earthquake Engineering*. Prentice Hall, Upper Saddle River, New Jersey, USA.
- Liu, W., Yamazaki, F., 2017. Extraction of collapsed buildings in the 2016 Kumamoto earthquake using multi-temporal palsar-2 data. *Journal of Disaster Research* 12 (2), 241–250.
- Liu, W., Yamazaki, F., Gokon, H., Koshimura, S., 2013. Extraction of tsunami-flooded areas and damaged buildings in the 2011 tohoku-oki earthquake from terrasar-x intensity images. *Earthquake Spectra* 29 (S1), S183–S200.
- Matsuoka, M., Nojima, N., 2010. Building damage estimation by integration of seismic intensity information and satellite l-band Sar imagery. *Remote Sens.* 2 (9), 2111–2126.
- Matsuoka, M., Yamazaki, F., 2004. Use of satellite Sar intensity imagery for detecting building areas damaged due to earthquakes. *Earthquake Spectra* 20 (3), 975–994.
- Miura, H., Midorikawa, S., Matsuoka, M., 2016. Building damage assessment using high-resolution satellite Sar images of the 2010 Haiti earthquake. *Earthquake Spectra* 32 (1), 591–610.
- Moya, L., Yamazaki, F., Liu, W., Chiba, T., 2017. Calculation of coseismic displacement from lidar data in the 2016 Kumamoto, Japan, earthquake. *Nat. Hazards Earth Syst. Sci.* 17 (1), 143–156.
- Moya, L., Marval Perez, L.R., Mas, E., Adriano, B., Koshimura, S., Yamazaki, F., 2018a.

- Novel unsupervised classification of collapsed buildings using satellite imagery, hazard scenarios and fragility functions. *Remote Sens.* 10, 296.
- Moya, L., Mas, E., Adriano, B., Koshimura, S., Yamazaki, F., Liu, W., 2018b. An integrated method to extract collapsed buildings from satellite imagery, hazard distribution and fragility curves. *International Journal of Disaster Risk Reduction* 31, 1374–1384.
- Moya, L., Yamazaki, F., Liu, W., Yamada, M., 2018c. Detection of collapsed buildings from lidar data due to the 2016 Kumamoto earthquake in Japan. *Nat. Hazards Earth Syst. Sci.* 18 (1), 65–78.
- Moya, L., Endo, Y., Okada, G., Koshimura, S., Mas, E., 2019a. Drawback in the change detection approach: false detection during the 2018 western Japan floods. *Remote Sens.* 11 (19).
- Moya, L., Zakeri, H., Yamazaki, F., Liu, W., Mas, E., Koshimura, S., 2019b. 3d gray level co-occurrence matrix and its application to identifying collapsed buildings. *ISPRS J. Photogramm. Remote Sens.* 149, 14–28.
- Muhari, A., Imamura, F., Arikawa, T., Hakim, A.R., Afriyanto, B., 2018. Solving the puzzle of the september 2018 Palu, Indonesia, tsunami mystery: clues from the tsunami waveform and the initial field survey data. *Journal of Disaster Research* 13, 1–3 sc20181108.
- Ozawa, S., Nishimura, T., Suito, H., Kobayashi, T., Tobita, M., Imakiire, T., 2011. Coseismic and postseismic slip of the 2011 magnitude-9 tohoku-oki earthquake. *Nature* 475, 373–376.
- Planet, 2018. **Disaster Data**. available at: <https://www.planet.com/disasterdata/> (Online; last accessed 11-May-2019).
- Rainforth, T., Wood, F., Jul 2015. **Canonical Correlation Forests**. arXiv e-Prints. arXiv:1507.05444.
- Rosu, A.-M., Pierrot-Deseilligny, M., Delorme, A., Binet, R., Klingner, Y., 2015. Measurement of ground displacement from optical satellite image correlation using the free open-source software micmac. *ISPRS J. Photogramm. Remote Sens.* 100, 48–59.
- Sassa, S., Takagawa, T., Jan 2019. Liquefied gravity flow-induced tsunami: first evidence and comparison from the 2018 Indonesia Sulawesi earthquake and tsunami disasters. *Landslides* 16 (1), 195–200.
- Shearer, P.M., 2009. **Introduction to Seismology**, 2nd edition. Cambridge University Press.
- Socquet, A., Hollingsworth, J., Pathier, E., Bouchon, M., 2019. Evidence of supershear during the 2018 magnitude 7.5 Palu earthquake from space geodesy. *Nat. Geosci.* 12, 192–199.
- Stumpf, A., Malet, J.-P., Delacourt, C., 2017. Correlation of satellite image time-series for the detection and monitoring of slow-moving landslides. *Remote Sens. Environ.* 189, 40–55.
- Takagi, H., Pratama, M.B., Kurobe, S., Esteban, M., Aránguiz, R., Ke, B., 2019. Analysis of generation and arrival time of landslide tsunami to Palu city due to the 2018 Sulawesi earthquake. *Landslides* 16, 983–991.
- Takita, K., Aoki, T., Sasaki, Y., Higuchi, T., Kobayashi, K., 2013. High-accuracy subpixel image registration based on phase-only correlation. *IEICE Trans. Fundamentals E86-A (8)*, 1925–1934.
- The AHA Centre, 2018. **Situation update no. 15 - final; M 7.4 earthquake & tsunami Sulawesi, Indonesia**. available at: <https://ahacentre.org/situation-update/situation-update-no-15-sulawesi-earthquake-26-october-2018/>.
- The European Space Agency, 2018. **Sen2Cor**. available at: <https://step.esa.int/main/third-party-plugins-2/sen2cor/> (Online; accessed 30-June-2019).
- Tong, X., Ye, Z., Xu, Y., Gao, S., Xie, H., Du, Q., Liu, S., Xu, X., Liu, S., Luan, K., Stilla, U., Oct 2019. Image registration with fourier-based image correlation: a comprehensive review of developments and applications. *IEEE Journal of Selected Topics in Applied Earth Observations and Remote Sensing* 12 (10), 4062–4081.
- Udías, A., Madariaga, R., Buforn, E., 2014. **Source Mechanisms of Earthquakes: Theory and Practice**. Cambridge University Press.
- Wong, A., Clausi, D.A., May 2007. Arrsi: automatic registration of remote-sensing images. *IEEE Trans. Geosci. Remote Sens.* 45 (5), 1483–1493.
- Xu, X., Li, X., Liu, X., Shen, H., Shi, Q., 2016. Multimodal registration of remotely sensed images based on Jeffrey's divergence. *ISPRS J. Photogramm. Remote Sens.* 122, 97–115.
- Yamazaki, F., Matsuoka, M., September 2007. Remote sensing technologies in post-disaster damage assessment. *Journal of Earthquake and Tsunami* 1 (3), 193–210.